LABORATORI NAZIONALI DI FRASCATI
SIS – Pubblicazioni

LNF–98/011(P)
16 Aprile 1998

A New Photoelectron Imager for X–Ray Astronomical Polarimetry

A. La Monaca[(1)], E. Costa[(2)], P. Soffitta[(2)], G. Di Persio[(2)], M. Manzan[(2)], B. Martino[(2)], G. Patria[(2)], G. Cappuccio[(3,1)], N. Zema[(4)]

(1) INFN, Laboratori Nazionali di Frascati, via E Fermi 40, P.O.B. 13, 00044 Frascati, Italy
(2) Istituto di Astrofisica Spaziale del CNR, via del Fosso del Cavaliere, 00133 Roma, Italy
(3) Istituto di Strutturistica Chimica del CNR, P.O.B. 10, 00010 Monterotondo Staz., Italy
(4) Istituto di Struttura della Materia del CNR, via del Fosso del Cavaliere, 00133 Roma, Italy

Abstract

A new photoelectron imager for X–ray astronomical polarimetry (PIAP) has been developed and tested at the Frascati laboratories (LNF–INFN). A charge–coupled device (CCD) is placed on one of the two conjugate foci of a Cassegrain reflective optics onto which are focused UV photons emitted by means of gas scintillation. This X–ray detector has been built to image the angular distribution of the photoelectron tracks, whose anisotropy measures the X–ray polarization. First tests, performed by using mixtures based on argon gas and benzene at low pressure, show events which are candidate tracks of photoelectrons and Auger electrons produced by a ^{55}Fe source.

PACS.: 95.55.Q, 95.75.H, 95.85.N, 07.85.F
Key words: X–ray high–energy astronomy; Polarimetry; Scintillation gas; Back–side illuminated CCD; Imaging detector

Submitted to
Nucl. Inst. & Meth. – Section A

Work supported by: INFN, Group V: PIAP experiment (45 AR–LNF); and partly by IAS–CNR on ASI contract.

1 – INTRODUCTION

X–rays emitted from celestial sources belonging to many of the most popular classes should be linearly polarized to a high degree, according to the widely accepted models. In many cases, the detection of the amount and angle of linear polarization and its dependence on the energy and time could be decisive for understanding the physical processes in the emitting cosmic source [1 – 4]. In practice, this has been proved for one source only (the Crab Nebula), with the OSO–8 satellite more than 20 years ago [5]. In 1998, the Spectrum–X–γ satellite will carry in orbit the first focal plane polarimeter (SXRP [6]) capable of extending the number of known sources from one up to 20 – 30. Although this is expected to rejuvenate the important sub–topic of X–ray astronomy, a great number of questions, mainly referring to low–luminosity galactic sources and the totality of the extragalactic sky, will still remain open. For this a significant development in the available instrumentation is still required. No substantial improvement in the sensitivity of an astronomical polarimeter can be expected in the framework of the conventional techniques, based on Bragg diffraction and Compton scattering. A more substantial improvement can be achieved by a detector with a space resolution sufficient to resolve the track of a photoelectron. Such a detector would combine the measurement of the point of interaction (required in the focus of an optics) with the simultaneous detection of the linear polarization of the photon by orientation of the track. The development of a new X–ray polarimeter based on the angular distribution of the photoelectron tracks in a gas is the target of the photoelectron imager for X–ray astronomical polarimetry (PIAP experiment). Unless more complex than the other experiments based on the same ideas, using CCDs [7, 8] or microgap chambers [9], the PIAP allows for the full exploitation of the available information and represents the ultimate application of this physical effect [10].

Photoelectron tracks produced by hard X–rays have been imaged for more than 70 years [11, 12]. Our goal is to build an X–ray polarimeter based on the photoelectron effect, sensitive in the soft–X–ray regime and self–triggered, for use on board space vehicles. In this regard we were careful to choose optical components having low UV absorption and a CCD having high UV quantum efficiency in order to maximize the sensitivity to the dim flash produced by a few keV photoelectrons.

2 – EXPERIMENTAL APPARATUS

Figure 1 is a schematic of the PIAP apparatus and Fig. 2 shows the experimental setup. Our detector consists of a gas cell (GSC) with a thick X–ray conversion region placed immediately behind a beryllium window and in front of a thinner scintillation region. An external Cassegrain optical system collects converted UV photons, which pass through a LiF window, and focuses them onto a CCD camera using an ultra–thinned and back–side illuminated CCD. Low–pressure gauges plus filters on the high–vacuum system and low–pressure gas system allow one to choose the appropriate gas mixture and pressure. Readout CCD electronics and an acquisition hardware/software system complete the instrumentation.

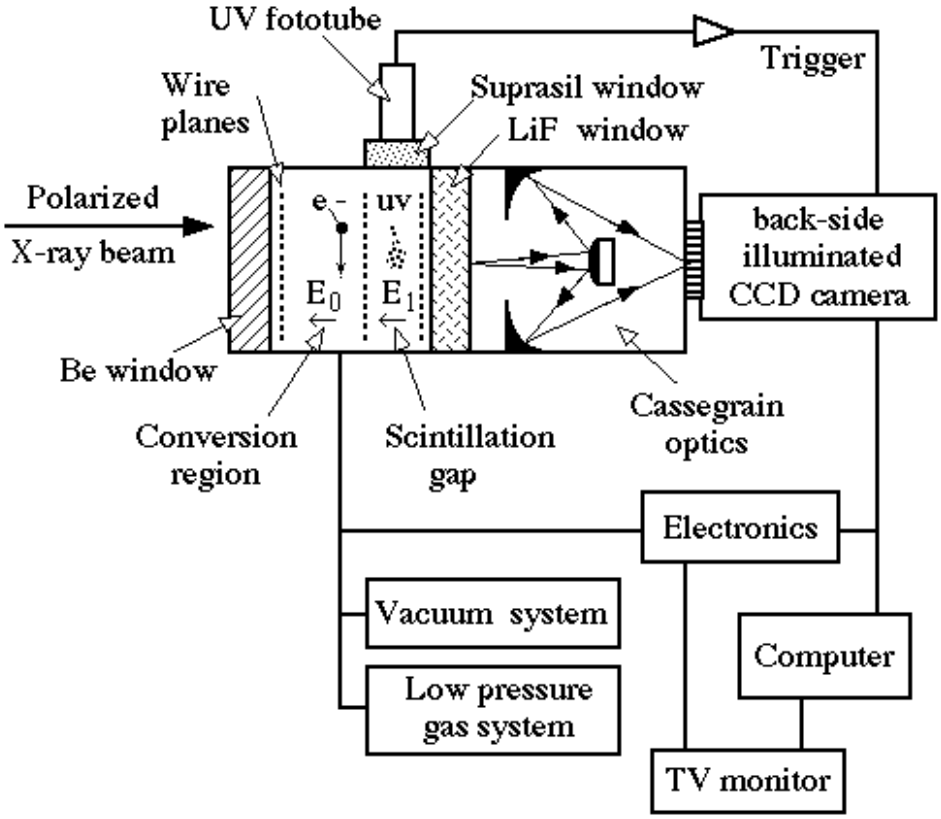

FIG. 1 – Schematic of the PIAP apparatus showing the gas scintillation chamber, the optical system and the CCD camera.

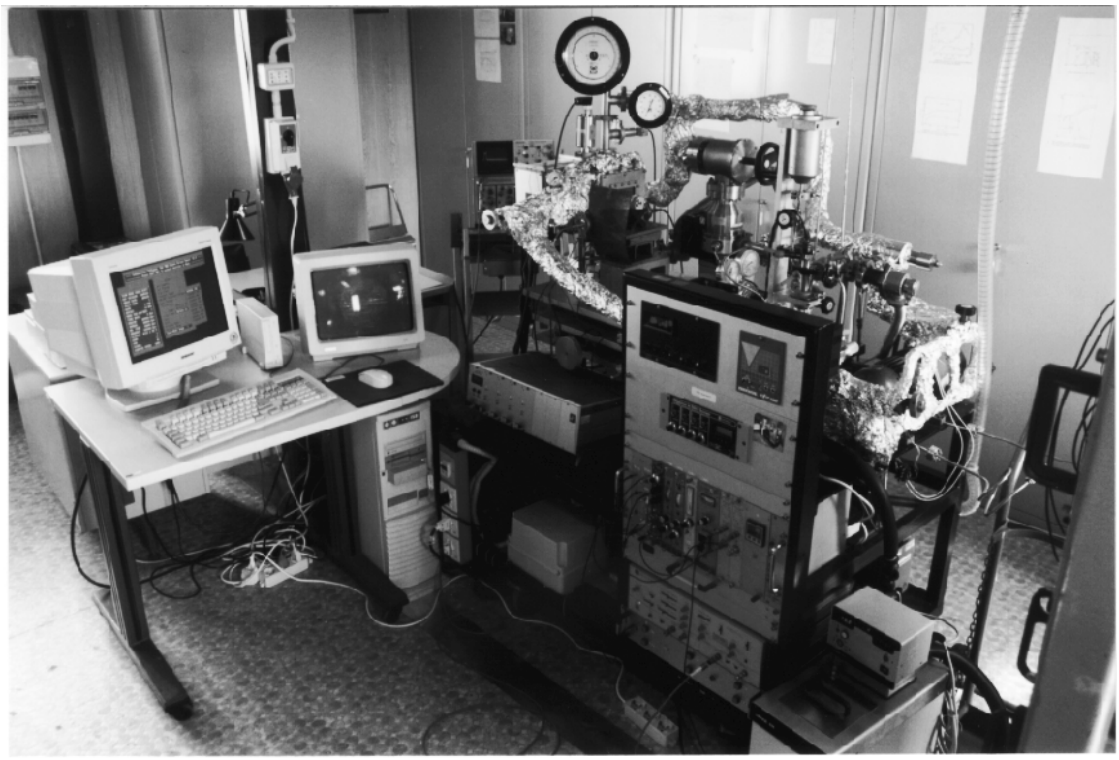

Fig. 2 – The experimental PIAP setup.

2.1 – Gas cell

The gas scintillation chamber (GSC) is defined by three parallel wire planes (or grids) placed behind the beryllium entrance window. Their effective area is 100x100 mm^2 and the gold plated copper wires are 0.1 mm in diameter, spaced with 1 mm of the pitch on each plane. The X–ray conversion region is defined by the first two wire grids, (the first grid could be replaced by the same beryllium window, insulated for supporting any electrical potential), whose distance can be determined in the range 10 – 30 mm to obtain a better X–ray absorption. The electron charge created in the gas in this region is guided without amplification by a homogeneous and uniform weak electric field, E_1, up to the contiguous photon scintillation gap. The gap is geometrically delimited by the third grid parallel to the second, and the high voltage that drops between them generates the appropriate scintillation field, E_2. The light emission produced in this region increases with gap size. Since the mean path of the electron charge is longer in a wider gap, more inelastic collisions, giving rise to scintillation light emitted by atoms in the excited state, occur in the path. Therefore, the intensity of the scintillation photons will be proportional to the total voltage drop of the gap, which is larger in a wider gap. This means that a thicker scintillation gap requires a higher operating voltage, with the possible risk of discharge, while the imaging properties worsen due to the deviation from planarity of light distribution. For these reasons, a set of calibrated spacers allows the gap size to be spaced in the range 3 – 10 mm. By using Ar (96 – 85%) + benzene (4 – 15%) gas mixtures and a ^{55}Fe X–ray source of 5.9 keV of energy, the first satisfactory experimental results were obtained by fixing the conversion region of the chamber at 15 mm and the gap size at 5 mm. The electric fields in the conversion region and in the gap were 400 V/cm and 1240 V/cm, respectively. Benzene/argon concentrations were calibrated using two high–precision gauges. The measurements were done at 18 ℃ and at a vapour pressure of 200 mbar.

Argon gas is relatively good for detecting polarized low–energy X–rays. It is also cheap and convenient for filling gas chambers, but its light emission peak lies at 126 nm, where detection is more difficult [13]. One way to shift its emission to a more convenient wavelength region is to take advantage of energy transfer phenomena, where argon acts as donor to an appropriate acceptor, such as benzene. Benzene vapour exhibits large absorption bands and relative emissions in the far UV photons [14]. One of the bands extends from about 100 nm to about 140 nm and covers the region of light emission of argon very well, with a relative quantum efficiency of absorption $\varepsilon \approx 60$ %[15].

Molecular excited states of higher energy can transfer energy to lower excited states through the interaction of the molecular electronic states with the vibration modes, while the doubly–exited states directly emit light at lower energy in a strong band. This band of benzene extends from 179 to 220 nm with one absolute maximum peak at 180 nm and another relative maximum at 200 nm, due to molecular transitions to the ground state of a singlet [14].

Scintillation photon flashes are collected by a Cassegrain optical system through a LiF window with a useful area of 60 x 60 mm^2, a thickness of 5 mm and 95 % transparency.

2.2 – Vacuum apparatus and low pressure gas system

The vacuum apparatus, gas system and GSC are manufactured with specific materials for UV technology. Figure 3 shows a schematic of the setup. The vacuum circuit consists of a system of mechanical and turbomolecular pumps with a molecular trap and Pirani and Penning vacuum gauges. The system components, valves and seal material were tested with a leak detector calibrated for a sensitivity of 10^{-10} (He)cm^3/sec. The system can be baked at 150 ^{o}C; but without baking, after 20 min the whole system can reach a pressure of 10^{-5} mbar, which is sufficient for our purposes.

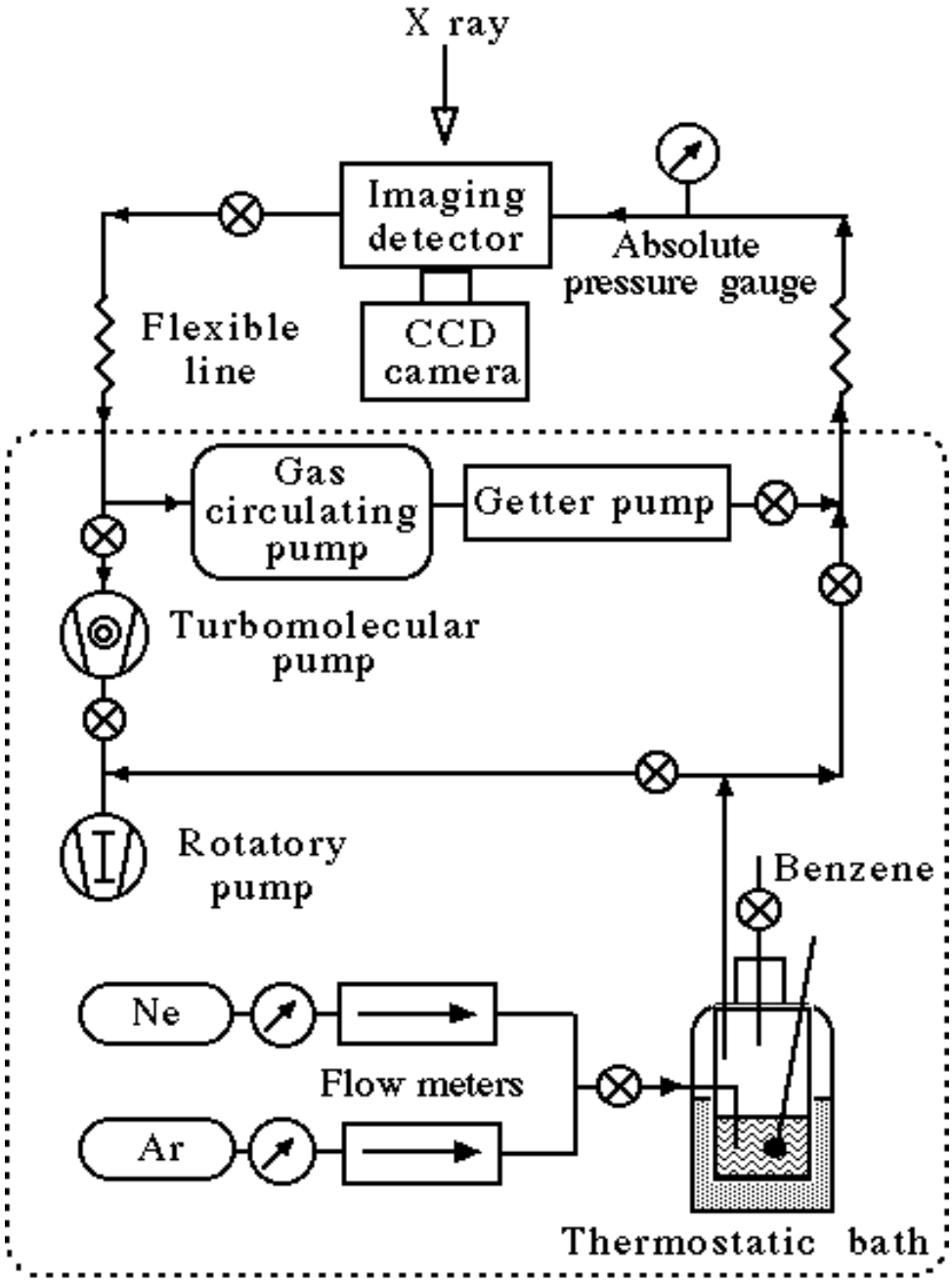

Fig. 3 – Vacuum apparatus and low–pressure closed circulating–gas system with getter pump and thermostatic bath.

Gas is circulated using a KNF Neuberger (N 86.3AV.12E) double–diaphragm pump, which works up to a limit pressure of 10^{-6} mbar. An Alphagas getter pump (Sorbal–10) inserted in the gas circuit removes most of the contaminants: oxygen, water, carbon monoxide and carbon dioxide, reducing their traces to less than 0.1 – 0.4 ppmv. These contaminants, due to the materials used for the wire–detector, i.e., vetroresin, epoxy resin, PVC cables, stain sealing, etc., have a dramatic effect on UV light emission, which in a short time can decrease the intensity level by a factor of four. The wire detector has therefore been placed inside a stainless steel chamber, connected to the gas closed circuit, where the gas is cleaned by being circulated for five minutes [16].

As many candidates detecting or shifting materials are below the critical temperature, we designed and manufactured a special evaporation glass–bulb to allow the injection of a controlled amount of vapour in the chamber. Therefore, the concentration of benzene in the gas mixture can be easily controlled by the temperature of the thermostatic bath, which regulates the relative organic vapour pressure.

2.3 – Cassegrain system

The optical system is based only on reflective mirrors, which is more efficient than refractive optics (used in other configurations [12]) for focusing UV light and forming optical images free of chromatic aberrations over all the desired energy band. As shown in Fig. 4, the system geometry is similar to a Cassegrain with two spherical mirrors, but is used in reversed mode in order to obtain demagnified images on the small area of the CCD. The device was tailor–made by French Optique de Precision J. Fichou. It has an external diameter of 75 mm and a total length of 210 mm. The primary mirror (S_1) is larger than the secondary (S_2) mirror. The latter, located in the geometrical centre of the optical system, forms the virtual object (GSC) for the primary mirror [17]. The mirror surfaces are spherical with different curvature radii: r_1 and r_2. The distance between the mirrors is d=90 and the distances from the mirrors to their respective focal planes are $d_1 = d_2 = 140$ mm. In the normal case, when an object is reflected by S_1 on the focal plane of S_2, the angular magnification is $m = \alpha/\beta = 6.57$. When the Cassegrain is used in reversed mode and the object is in front of S_2, the image on the focal plane of S_1 is angularly demagnifed by 1/m (see Fig. 4). The relative aperture of the system is 0.25 (as viewed by the CCD). The reflecting mirror surfaces are made of aluminium, whose reflectivity is about 90% for UV light in the region of interest. Nevertheless, it should be noted that the greatest waste of light is not due to the optical elements but to the geometrical coupling determined by the solid angle subtended by the CCD surface.

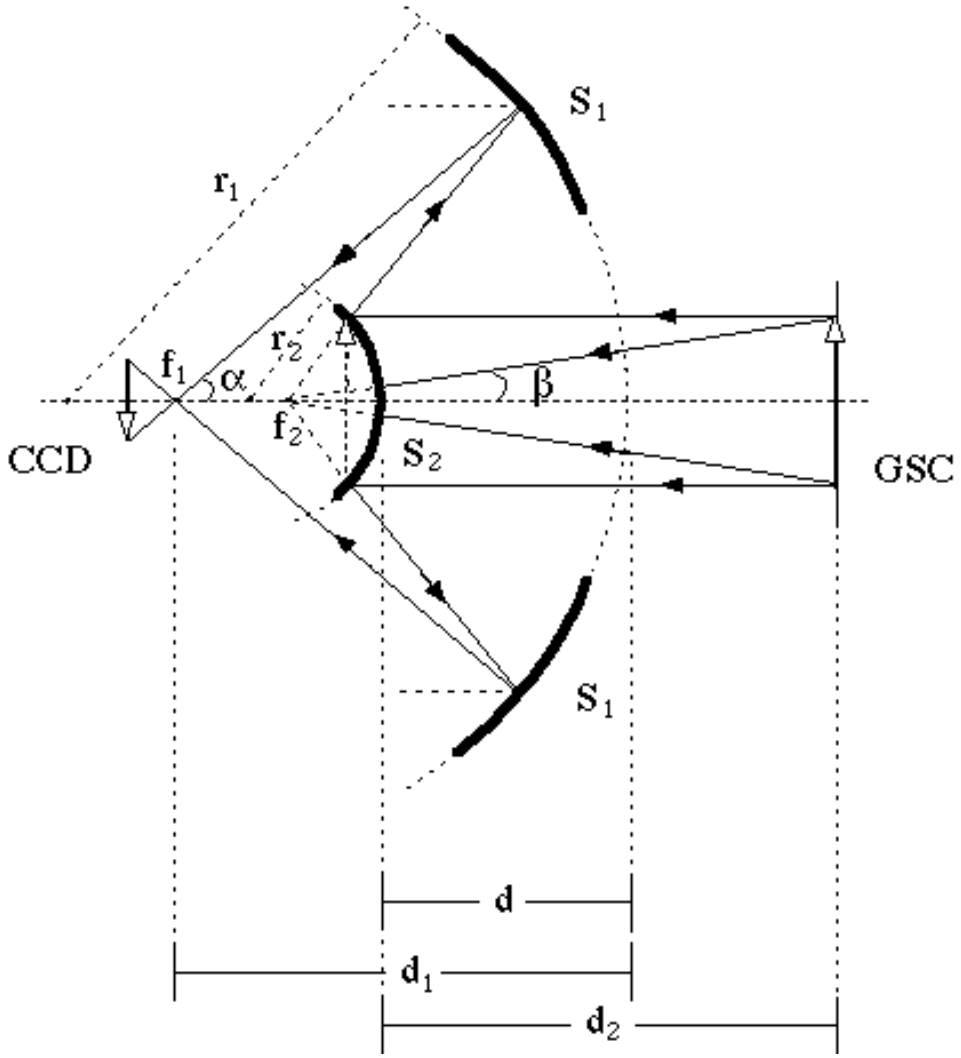

FIG. 4 – Diagram of the reversed Cassegrain optical system (not in scale) with S_1 and S_2 spherical mirrors, with different curvature radii: r_1 and r_2; d = 90 mm and $d_1 = d_2$ = 140 mm are the distances between the mirrors and the distances between the mirrors and the relative focal planes; $m=\alpha/\beta=6.57$ is the angular magnification. An object on the focal plane of S_2 (Cassegrain used in reversed mode) will be angularity demagnifed by 1/m onto an image on the focal plane of S_1.

2.4 – CCD Camera for UV light image

The CCD camera has been designed to detect UV light images and uses a special optical charge–coupled device. It consists of a detector made of silicon material arranged in a m × n pixel matrix (rows by columns) [18]. Since the silicon CCD generates undesired thermal charges at a rate dependent on operating temperature, they are cooled. An electronic system (Peltier effect) is sufficient for reducing the dark current to a negligible level, with a statistical uncertainty of ≈ 2 – 3 electrons/pix, and as high as 10^5 electrons/pix [19, 20].

The CCD sensitivity depends on how efficiently the photons are collected. In a standard CCD, the light passes to the active silicon layer through the electrodes, made of polysilicons and strongly absorbent of UV and blue light. One way to extend the response

to shorter wavelengths is to create an open–pixel device, in which only part of the pixel (virtual electrode) at each pixel site would directly absorb photons. However, the most effective way to overcome the surface absorption losses is the back–side–thinning.

The CCD is thinned to about 10 μm by etching its back–side and is illuminated from the back. All the photons can now penetrate to the active collection site without large absorption losses. The addition of an anti–reflection coating enables a 100% quantum efficiency to be obtained over the visible–light range. A potential drawback in using a back–illuminated CCD is the charge diffusion from the back–side silicon into the interface states of natural SiO_2 and the consequent reduction in efficiency. The reduction is prevented in our case by implantation of local sub–surface doping boron ions. The electric effect consequent to the implantation helps to hold the electrons in place [20, 21].

We have used a Thomson–CSF, TH7395 AVRX N–B, back–side–illuminated CCD. It consists of a matrix of 19×19 μm^2, 512×512 pixels, with ≈ 100% aperture. The image area is 9.73×9.73 mm^2. The maximum image rate of the matrix readout is obtained at a 14–MHz pixel frequency using two subsequent readout registers, located on the opposite side of the sensible optical region. Each register receives half an image, which is transferred line–by–line in parallel sequence from 1 to 258 on the top readout register and from 516 to 259 on the bottom readout register. Similarly, each readout register transports serially half a charge from 1 to 258 pixels to the right output and half from 516 to 259 pixels to the left output. The maximum charge capability of the device is 4.5×10^5 electrons per pixel in saturation regime, and the noise level is 20 electrons per pixel at a thermostatic temperature of 20 ^{o}C. Nevertheless, for detecting low light levels and for obtaining images with the best linearity (1%) and without localized singular spikes, it is preferable to use a low–frequency configuration with only one activated readout register and only one output. In such a case, the image is inverted with respect to a real object and the noise level is limited to only 4 electrons per pixel [20]. In this configuration, according to our measurements, the UV spectral response curve of the sensor has a quantum efficiency of about 30% at wavelength 1800 Å. No radiation damage was recorded because the photons of this energy cannot reach the pixel electrode polysilicon structure and thereby create traps for the charge inside it [22].

The sensor is mounted on the Thomson–CSF, TH79KA95, CCD camera. The analog output is matched with a 75–Ω impedance to drive an 8– or 10–bit ADC. Digitized bit outputs are compatible with the digital inputs of the frame grabber. With a precision of 10 bits the digitizer allows accurate measurement of the light intensity over a large dynamic range. The video standard signal is displayed on a TV monitor, the digitized images can be transferred to a file and saved on an IBM–PC hard disk [20]. The camera head is adapted to cool the CCD by the Peltier effect. A versatile shutter is used to control the integration time and the read mode.

A self–triggering detector is fundamental in X–ray astronomy because when an X–ray arrives it is unknown, and also the non–X–ray background counting rate can be orders of magnitude higher than that of the source. Thus on the gas scintillation chamber we have accommodated a quartz window and a multichannel photomultiplier tube (Hamamatsu H 6665 assembled version) for self–triggering.

The use of an external photomultiplier tube, controlling the CCD image acquisition, allows on–board background rejection based on the signal amplitude and on the burst length from a long–track particle event. For performing the background rejection, a multi–anode photomultiplier tube can be also used. Due to the different solid angles covered by each electrode in the tube, a rough event positioning can be achieved.

3 – RESULTS AND DISCUSSION

The measurement of polarization from the orientation of the photoelectron track is limited by three types of effects:

1) The photoelectron is ideally distributed with a $\cos^2\vartheta$ law around the direction of the electric vector E of the impinging photon beam, but other effects compete with this, particularly the less sharp distribution of the photoelectrons *p*, *d*, etc. [23].
2) The electron, created by the photoelectric effect, is scattered by the collisions with the atoms of the gas, which causes part of the information on the direction to be lost.
3) Projection effects can occur because the photoelectron is not emitted exactly on a plane perpendicular to the photon and because the plane of the detector may not be exactly perpendicular to the photon beam itself. Moreover, part of the track is made up of Auger electrons, which do not retain any information on the photon polarization.

Projection effects can be accounted for by appropriate geometrical corrections, as shown below. The other effects will reduce the sensitivity of the polarimeter but will not destroy it since the track will preserve an asymmetry that retains information on the original direction of the photoelectron. In the following, we present preliminary measurements showing that our instrument can resolve photoelectron tracks and measure their extension and orientation in the plain perpendicular to the X–ray beam.

We performed measurements with X–rays of energy E_i = 5.9 keV emitted from a ^{55}Fe radionuclide source. The source can be moved 12 – 72 mm orthogonally to the xy plane of the polarimeter. The X–ray photons, travelling along the z–direction, are not polarized (an X–ray polarized source for testing is under construction). Therefore, the electric field E vectors of the electromagnetic wave, which always lies on the azimuth plane and orthogonal to the direction of propagation of the incident X–rays, are symmetrically arranged around this direction.

However, each incident photon *i* can be localized by the polar φ and α coordinates, as shown in Fig. 5, and the polarization electric field vector E_i is univocally determined by the ϑ_i azimuth angle on the x_iy_i plane. In this case, the polarization components of the electric field E_i can be transformed on the xy detection plane of the polarimeter by using the unitary matrix of rotations through the angles α and φ around the z and y axes, respectively:

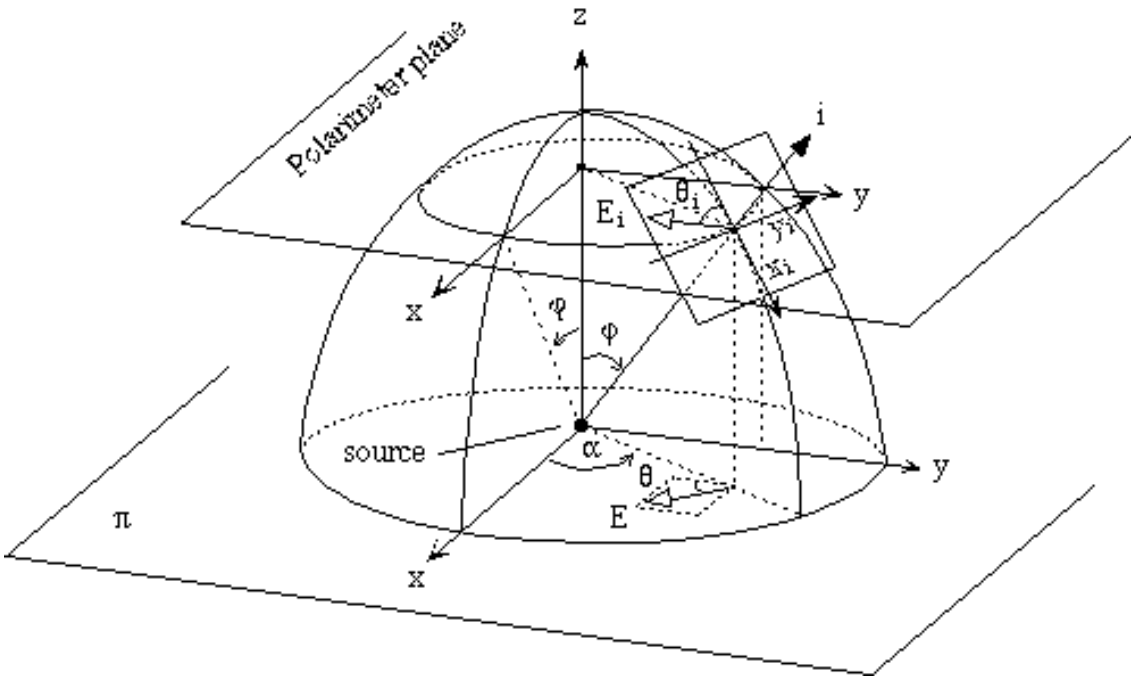

FIG. 5 – Schematic representing the experimental geometry of X–rays incident on the polarimeter. The X–ray source is placed in the origin of the xyz coordinates. The polarimeter plane, cutting the z–axis at distances of 12 – 72 mm, is parallel to the xy source. The incident photon *i* is defined by the polar coordinates α and φ. The polarization vector lies on the plane orthogonal to the propagation direction of the photon *i*, and makes an angle ϑ_i with x–axis. A double rotation through the α and φ angles around the z and y axes transforms the axis coordinates of the polarization vector *i* into the axis coordinates of the polarimeter. For clarity, the image of the polarization vector is represented not on the polarimeter plane but on the π plane.

$$\begin{pmatrix} E_x \\ E_y \\ E_z \end{pmatrix} = \begin{pmatrix} \cos\varphi & 0 & \sin\varphi \\ 0 & 1 & 0 \\ -\sin\varphi & 0 & \cos\varphi \end{pmatrix} \cdot \begin{pmatrix} \cos\alpha & -\sin\alpha & 0 \\ \sin\alpha & \cos\alpha & 0 \\ 0 & 0 & 1 \end{pmatrix} \cdot \begin{pmatrix} E_{ix} \\ E_{iy} \\ 0 \end{pmatrix}$$

$$\begin{pmatrix} E_x \\ E_y \\ E_z \end{pmatrix} = \begin{pmatrix} \cos\varphi & 0 & \sin\varphi \\ 0 & 1 & 0 \\ -\sin\varphi & 0 & \cos\varphi \end{pmatrix} \cdot \begin{pmatrix} \cos\alpha \cdot E_{ix} - \sin\alpha \cdot E_{iy} \\ \sin\alpha \cdot E_{ix} + \cos\alpha \cdot E_{iy} \\ 0 \end{pmatrix}$$

$$\begin{pmatrix} E_x \\ E_y \\ E_z \end{pmatrix} = \begin{pmatrix} \cos\varphi \cdot (\cos\alpha \cdot E_{ix} - \sin\alpha \cdot E_{iy}) \\ \sin\alpha \cdot E_{ix} + \cos\alpha \cdot E_{iy} \\ -\sin\varphi \cdot (\cos\alpha \cdot E_{ix} - \sin\alpha \cdot E_{iy}) \end{pmatrix}$$

The E_z component is orthogonal to the xy polarimeter plane and is therefore null. For the other two components, E_x and E_y, we can write:

$$E_x = (E_i \cos\vartheta_i \cos\alpha - E_i \sin\vartheta_i \sin\alpha) \cos\varphi,$$
$$E_y = (E_i \cos\vartheta_i \sin\alpha + E_i \sin\vartheta_i \cos\alpha),$$

We transform the ratio E_y/ E_x by using easy trigonometric formulas in the simple relation:

$$\tan\vartheta = \tan(\vartheta_i+\alpha)\sec\varphi \qquad (1)$$

For fine collimated sources, in which $\varphi = 0°$ and $\alpha = 0°$, this formula gives $\vartheta = \vartheta_i$. Otherwise, the experimental angle ϑ, left by the photoelectron track, is different from the polarization angle ϑ_i, which can be evaluated from (1) if α and φ are known.

The wire detector is filled with a mixture of argon (96 – 85 %) and benzene (4 – 15 %) as a wavelength shifter. In order to expand and properly visualize the track, we used low–pressure gas (50 – 500 mbar). Images were collected with a high counting rate, selecting off–line those which contained the image of a photon event, because an external trigger signal was not available at the time. As a consequence, we have a limited number of events for each test run. In some cases (Fig. 6) we have many different types of events in the same frame. The most intense track is generated by photoelectrons, ejected from the weakly bounded outer orbital (E_b =15.7 – 326.3 eV of energy) of the argon atom, which received a residual kinetic energy of $E_i - E_b$ keV.

In the case of spark events, the images show a brightened grid, which we use to produce a calibrated reference frame for the X–ray events. In some cases, we see bright, structured images, which we identify with tracks of the events following the detection, namely photoelectrons of 2.7 or 5.9 keV stopping in the gas, plus Auger electrons of 3 keV or a few eV. Figure 7 shows some of these double events. The peaks number 1 with comparable brightness represent an event with one ≈ 3–keV photoelectron plus a ≈ 3–keV Auger electron. The physical extension of these tracks is of the order of a grid pitch of 1 mm, which is an order of magnitude compatible with the extrapolated practical range of electrons in argon (3.8 mm for 6 keV and 1.25 mm for 3 keV of energy at 200 mbar of pressure) [23]. For the calculation we used the semi–empirical formula given by Isked [24], valid with 25% of accuracy in the energy range between 20 eV and 10 keV:

$$\ln[(Z/A)\, R_{ex}] = -4.5467 + 0.31104 \ln E + 0.07773 \ln^2(E) \qquad (2)$$

where R_{ex} = extrapolated range (μm cm^{-2}), Z / A = charge to mass ratio for the absorber, E = energy in eV.

These double structures can be made more evident by using the contour lines traced at z = const. (intensity) on the xy detection plane. The graphic scale is in pixel units and has to be multiplied for the optical magnification experimental factor m = 6.57 to obtain the values in real space**.** Following this graphic procedure we have analyzed many significant events, some of which are described below.

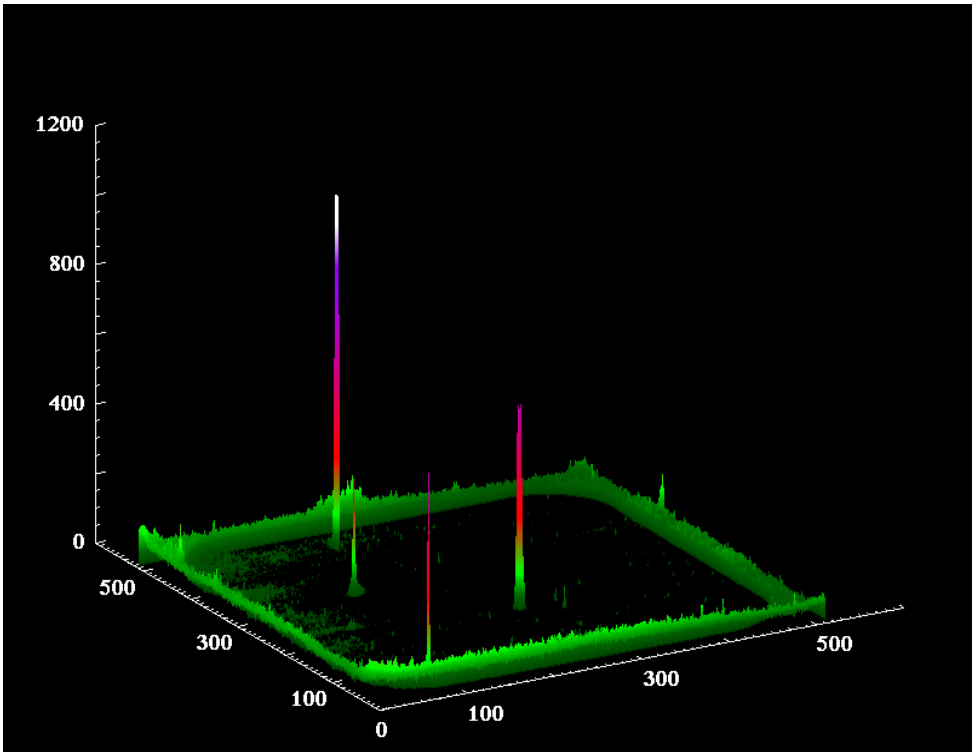

FIG. 6 – Three–dimensional track images of photoelectrons plus Auger electrons of around 3 keV, generated by a 5.9–keV X–ray of ^{55}Fe. The intensity increases according to the colour scale: green, orange, red, violet, white.

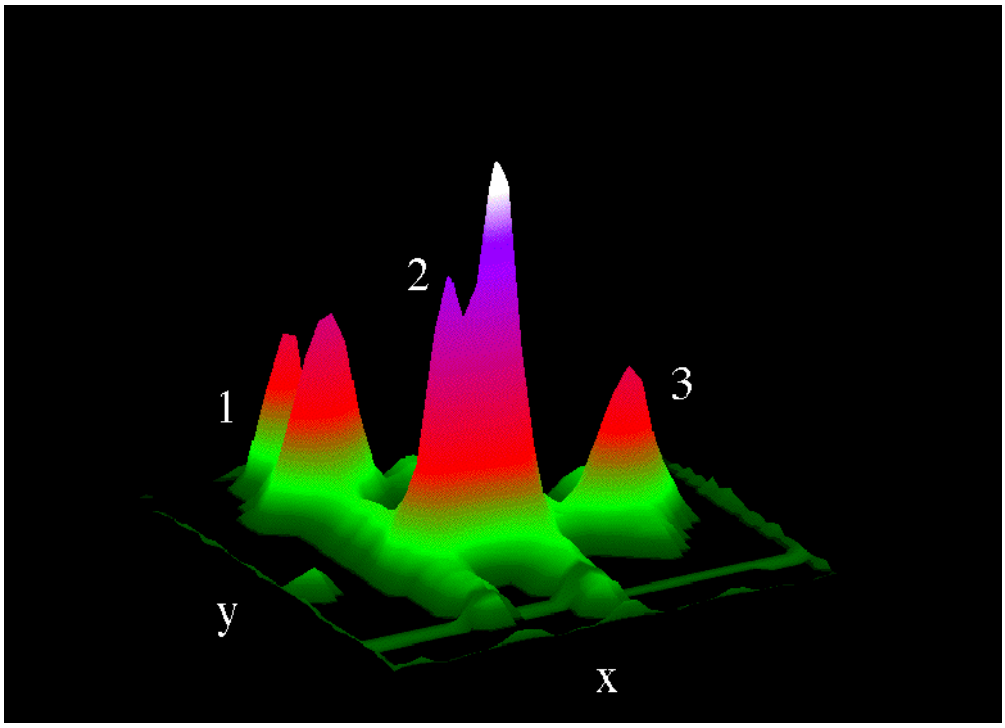

FIG. 7 – Structured images of double events. The event number 1 with double peaks of comparable brightness represents an event with one ≈ 3–keV photoelectron plus a ≈ 3–keV Auger electron. The physical extension of the tracks is of the order a grid pitch (shown in green) of 1 mm.

In Figs. 8 and 9 we can see asymmetric double structures having two spots of different brightness and belonging to a single event.

The small spot on the bottom of Fig. 8 as the start of the track which coincides with an Auger electron of a few tens of eV. The brighter spot, which is about 0.80 ± 0.03 mm from the previous one on the GSC plane, was identified as the photoelectron track carrying a residual energy of about 3 keV and information on the polarization direction. The symmetry contour of the photoelectron spot suggests that it is generated by an X–ray photon travelling in the x–direction with an inclination angle $\varphi \approx 0^o$ and an angle $\alpha \approx 0^o$. From formula (1) the polarization angle is $\vartheta = \vartheta_i = 70^o \pm 0.05^o$. Of course, this error is only the propagation of the errors on the determination of the peak positions and is much smaller than the "true" error, which is mainly due to electron scattering. This could only be determined by complex calculations, such as in [25], or from calibration with a parallel, 100% polarized beam.

The peaks of Fig. 9 are separated by about 1.60 ± 0.03 mm. The small spot on the right represents the starting point of the track with an Auger electron of 326 eV. The brighter asymmetric elongated spot on the left represents the projection of the photoelectron track on the polarimeter plane, carrying the residual energy $E_i - E_b = 5.57$ keV and the information about the polarization direction. We evaluated an angle $\alpha = 169.2^o \pm 0.1^o$, while the inclination angle was calculated to be $\varphi = -5^o \pm 1.5^o$. The large error on this measurement is due to the contribution of the absorption region which is thick with respect to the source–polarimeter distance. Therefore, from (1) we obtain an angle $\vartheta = 175.2^o \pm 0.05^o$ and a polarization angle $\vartheta_i = 6^o \pm 0.1^o$.

In the case of single spots, due to photoelectrons, which show a significant apparent polarization component in the x–axis direction generated by an X–ray travelling in the z–axis direction, we found tracks strongly inclined. For example, we found a strongly asymmetric track with a strong inclination angle $\varphi = 15^o \pm 3^o$ (source at maximum distance), extending for about 1.06 ± 0.03 mm from one side to one other. The starting point of the photoelectron track is in an angle $\alpha = 53.2^o \pm 0.1^o$ and since the angle $\vartheta = 87^o \pm 0.05^o$ is measured, the polarization angle is $\vartheta_i = 33.7^o \pm 0.1^o$.

In general, we can observe that the extension of the tracks is smaller than the extension given by [24]; this is because the extrapolated practical range in a β–experiment corresponds to a distance where the electron current is very low. On the other hand, since the specific ionization of the track $dE/dx \propto 1/T$, where T is the kinetic energy of the photoelectron, it is likely that the first part of the track has an insufficient number of electrons to provide the required brightness. Nevertheless, the fact that we detect tracks within a factor of two relative to the value reported in [24] shows that the PIAP has achieved a really good efficiency for low–ionization–density tracks.

Designs, graphics, images and data analysis were produced with Mathematica, a software system developed by Wolfram Res. Inc., USA, and IDL, Interactive Data Language (V. 4.0), a software package for the interactive analysis and visualization of data, developed by Research Systems Inc., USA.

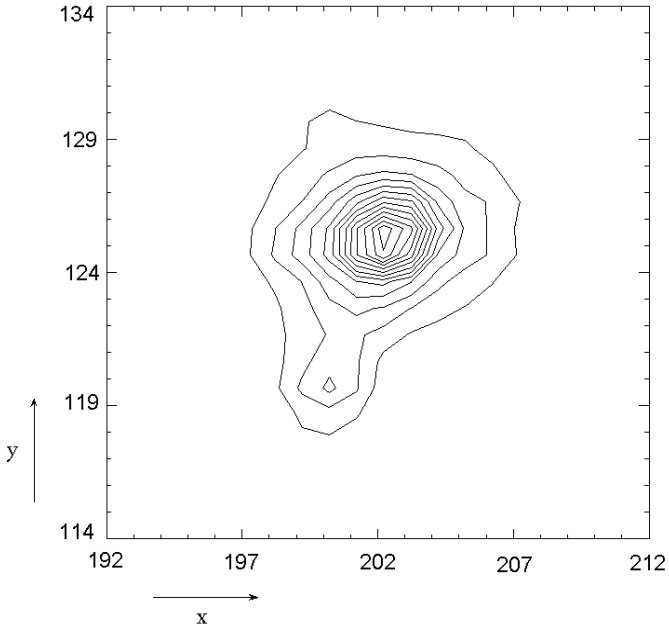

FIG. 8 – Asymmetric double structure, whose peak distance is ≈ 0.80 ± 0.03 mm. The small spot of an Auger electron of a few eV, on the bottom of the figure, is the start of the track. The brighter, elongated spot of the track of the photoelectron carrying the residual energy is at the top. The photoelectron track with the symmetric contour suggests that the X–ray photon travels along the x–axis with $\varphi \approx 0^o$ and $\alpha \approx 0^o$. The direction of the polarization is $\vartheta_i = 70^o \pm 0.05^o$.

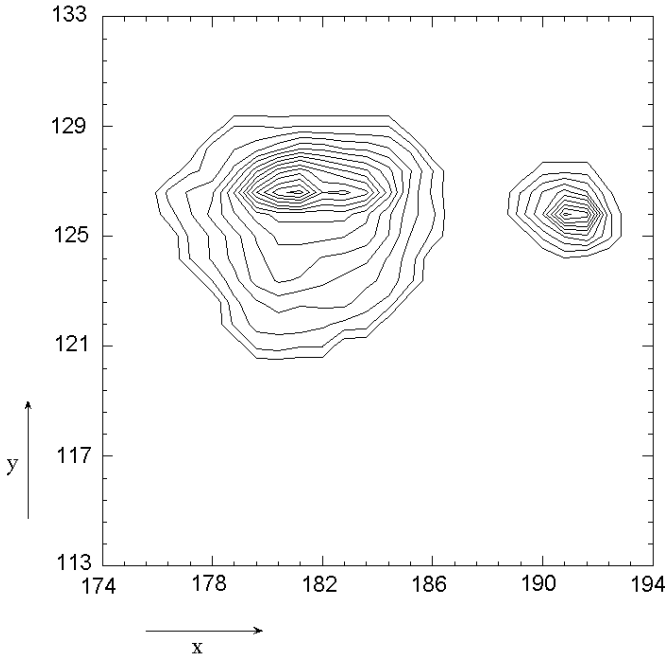

FIG. 9 – Another asymmetric double structure, whose peaks are 1.60 ± 0.03 mm from each other on the GSC plane. The small spot on the right can be identified as the start of the track with a 326–eV Auger electron. The brighter, asymmetric, elongated spot on the left represents the track of the photoelectron carrying the residual energy and information on the direction of the polarization, whose angle $\vartheta_i = 6^o \pm 0.1^o$ has been detected ($\vartheta = 175.2^o \pm 0.05^o$, $\alpha = 169.2^o \pm 0.1^o$ and $\varphi = 6^o \pm 3^o$, see text).

4 – CONCLUSIONS AND FUTURE DEVELOPMENTS

The measurements in the previous section show that:

i) the PIAP can detect X–ray photons;
ii) the photons produce extended tracks in the gas;
iii) the extension of the tracks is consistent with the extension of the range of the photoelectrons;
iv) the tracks are significantly asymmetric.

All these facts demonstrate that we have built an instrument capable of measuring the polarization of photons.

In conclusion, a new kind of X–ray photoelectron imager for astrophysical purposes based on the angular distribution of the photoelectron tracks has been developed. Ultraviolet photons produced by scintillation in an argon–benzene gas mixture at low pressure have been detected through a reversed Cassegrain optics by a back–side–illuminated CCD. By using a ^{55}Fe–source, X–ray photoelectron and Auger electron tracks have been imaged. The high sensitivity of the new X–ray instrumentation allows a single track of a photoelectron from a single event to be imaged and the X–ray polarization direction to be determined.

These first results should lead to further developments. The main improvement is expected from the use of low–Z gas mixtures, which will allow a better stopping power vs. scattering ratio and provide "straighter" tracks that will retain the information on the photoelectron emission much better. Moreover, the main process will be absorption on an *s*–electron, which retains intrinsically cleaner information on the polarization of the parent photon. With higher Z, the interaction will mainly involve *p*–electrons, which create photoelectrons with a less modulated distribution. The PIAP is conceived for use with Ne–based mixtures, but this development has not yet been implemented because of the many difficulties connected with the short wavelength of the neon scintillation (about 87 nm) [26].

We also intend to improve our analysis by searching for information from the total luminosity of the tracks. When we achieve an unambiguous identification of the events, we shall further develop the procedure for quantifying the anisotropy of tracks and their orientation in space.

5 – ACKNOWLEDGEMENTS

We should like to thank M. Brolatti of ISM–CNR, M. Frutti of IAS–CNR for the mechanical design, Dr. M. Lemonnier of LURE for his suggestions and help during the Cassegrain optical system development, Dr. M. Castellano and Dr. F. L. Fabbri of LNF–INFN for their support.

This work has been funded by Group V of INFN (PIAP experiment, 45 AR–LNF) and partly by IAS–CNR on ASI contract.

REFERENCES

[1] Yu.N. Gnedin and R.A. Sunyaev: Astr. & Ap. 36, 379 (1974).

[2] P. Meszaros, R. Novick, G.A. Chanan, M.C. Weisskopf and A. Szentgyörgy: Ap. J. 324, 1056 (1988).

[3] R.F. Stark and P.A. Connors: Nature 266, 429 (1977).

[4] R.A. Sunyaev and L.G. Titarchuk: Astr. & Ap. 143, 374 (1985).

[5] M.C. Weisskopf, E.H. Silver, H.L. Kestenbaum, K.S. Long and R. Novick: Ap. J. (Letters) 220, L 117 (1978).

[6] P. Kaaret, J. Schwartz, P. Soffitta , J. Dwyer, P. Shaw, S. Hanany, R. Novick, R. Sunyaev, I.Y. Lapshov, E.H. Silver, K.P. Ziock, M.C. Weisskopf, R.F. Elsner, B.D. Ramsey, E. Costa, A. Rubini, M. Feroci, L. Piro, G. Manzo, S. Giarrusso, A.E. Santangelo, L. Scarsi, G.C. Perola, E. Massaro, G. Matt: SPIE 2010, 22 (1993).

[7] G. Buschorn, R. Kotthaus, W. Kufner, W. Rössl, M. Rzepka, K.H. Schmidt, H. Genz, H.D. Gräf, P. Hoffman–Stascheck, U. Nething, A. Richter, W.R. Dix, G. Illing, M. Lohmann, J. Pflüger, B. Reime, L. Schildwächter: Nucl. Inst. & Meth. A 346, 578 (1994).

[8] H. Tsunemi, K. Hayashida, K. Tamura, S. Nomoto, M. Wada, A. Hirano and E. Miyata: Nucl. Inst. & Meth. A 321, 629 (1992).

[9] P. Soffitta, E. Costa, E. Morelli, R. Bellazzini, A. Brez, R. Raffo: SPIE 2517, 156 (1995).

[10] E. Costa, Proceedings (Multifrequency Behaviour of High Energy Cosmic Sources, 1996, eds. F. Giovannelli and L. Sabau–Graziati): Mem. SAIt. 67, 595 (1996).

[11] H.O. Auger: Inst. Soc. Am. Trans. 6, 311 (1966).

[12] R.A. Austin, T. Minamitani, B.D. Ramsey: SPIE 2010, 118 (1993).

[13] M. Suzuki and S. Kubota: Nucl. Inst. & Meth. 164, 197 (1979).

[14] J.N. Murrell: The Theory of the Electronic Spectra of Organic Molecules (J. Wiley and Sons Inc, New York, 1963).

[15] G. Charpak, S. Majewski, G. Melchart, F. Sauli, and T. Ypsilantis, Nucl. Inst. & Meth. 164 (1979) 419; A. Breskin, A. Cattai, G. Charpak, A. Peisert, A. Policarpo and F. Sauli: IEEE Trans. Nucl. Sci. NS–28, 429 (1981).

[16] G. Hubricht, K. Kleinknecht, E. Muller, D. Pollmann and E. Teupe: Nucl. Inst. & Meth. 228, 327 (1985).

[17] W.J. Smith: Modern Optical Engineering (Mc Graw–Hill Book Co., New York, 1966).

[18] J.D.E. Beynon, D.R. Lamb: Charge–coupled devices and their applications (Mc Graw–Hill Book Co., London, 1980).

[19] Princeton Instruments, Catalog of High performance Cameras, (1994).

[20] Thomson–CSF, CCD Data Book, 1988; and Thomson–CSF, TH79KA95 User guide (1992).

[21] C. Castelli, A. Wells, K. McCarthy and A. Holland: Nucl. Inst. & Meth. A 310, 240 (1991).

[22] A. La Monaca , P. Ottonello, M. Piacentini, G.A. Rottigni and N. Zema: Nucl. Inst. & Meth. A 292 (1990) 191.

[23] A.M. Afasanév, R.M. Inmamov, E.M Phasaev, V.N. Peregudov and M.I. Abdullaev: Soviet Physics of Solid State, 30, 1004 (1988).

[24] H. Isked, J.W. Cunningham and D.E. Watt: Phys Med. Biol., 28, 535 1983).

[25] D.C. Joy: Monte Carlo Modeling for Electron Microscopy and Microanalysis (Oxford University Press, 1995).

[26] A.H. Compton and S.K. Allison: X–Rays in Theory and Experiment (D. Van Nostrand Co., Princeton, New Jersey, 1957).